The Meteoritical Society

Meteoritics & Planetary Science 1–15 (2024)
doi: 10.1111/maps.14139

Hydrogen in magnetite from asteroid Ryugu

J. ALÉON[1]*, S. MOSTEFAOUI[1], H. BUREAU[1], D. VANGU[1], H. KHODJA[2], K. NAGASHIMA[3], N. KAWASAKI[4], Y. ABE[5], C. M. O'D. ALEXANDER[6], S. AMARI[7,8], Y. AMELIN[9], K. BAJO[4], M. BIZZARRO[10], A. BOUVIER[11], R. W. CARLSON[6], M. CHAUSSIDON[12], B.-G. CHOI[13], N. DAUPHAS[14], A. M. DAVIS[14], T. DI ROCCO[15], W. FUJIYA[16], R. FUKAI[17], I. GAUTAM[18], M. K. HABA[18], Y. HIBIYA[19], H. HIDAKA[20], H. HOMMA[21], P. HOPPE[22], G. R. HUSS[3], K. ICHIDA[23], T. IIZUKA[24], T. R. IRELAND[25], A. ISHIKAWA[18], S. ITOH[26], N. T. KITA[27], K. KITAJIMA[27], T. KLEINE[28], S. KOMATANI[23], A. N. KROT[3], M.-C. LIU[29,30], Y. MASUDA[18], M. MORITA[23], K. MOTOMURA[31], F. MOYNIER[12], I. NAKAI[32], A. NGUYEN[33], L. R. NITTLER[6], M. ONOSE[23], A. PACK[15], C. PARK[34], L. PIANI[35], L. QIN[36], S. S. RUSSELL[37], N. SAKAMOTO[38], M. SCHÖNBÄCHLER[39], L. TAFLA[29], H. TANG[29], K. TERADA[40], Y. TERADA[41], T. USUI[17], S. WADA[4], M. WADHWA[42], R. J. WALKER[43], K. YAMASHITA[44], Q.-Z. YIN[45], T. YOKOYAMA[18], S. YONEDA[46], E. D. YOUNG[29], H. YUI[47], A.-C. ZHANG[48], T. NAKAMURA[49], H. NARAOKA[50], T. NOGUCHI[26], R. OKAZAKI[50], K. SAKAMOTO[17], H. YABUTA[51], M. ABE[17], A. MIYAZAKI[17], A. NAKATO[17], M. NISHIMURA[17], T. OKADA[17], T. YADA[17], K. YOGATA[17], S. NAKAZAWA[17], T. SAIKI[17], S. TANAKA[17], F. TERUI[52], Y. TSUDA[17], S. WATANABE[20], M. YOSHIKAWA[17], S. TACHIBANA[53], and H. YURIMOTO[4]

[1]Institut de Minéralogie, de Physique des Matériaux et de Cosmochimie, Sorbonne Université, Museum National d'Histoire Naturelle, CNRS UMR 7590, IRD, Paris, France
[2]Université Paris-Saclay, CEA, CNRS, NIMBE, LEEL, Gif-sur-Yvette, France
[3]Hawai'i Institute of Geophysics and Planetology, University of Hawai'i at Mānoa, Honolulu, Hawaii, USA
[4]Department of Natural History Sciences, Hokkaido University, Sapporo, Japan
[5]Graduate School of Engineering Materials Science and Engineering, Tokyo Denki University, Tokyo, Japan
[6]Earth and Planets Laboratory, Carnegie Institution for Science, Washington, DC, USA
[7]McDonnell Center for the Space Sciences and Physics Department, Washington University, St. Louis, Missouri, USA
[8]Geochemical Research Center, The University of Tokyo, Tokyo, Japan
[9]Guangzhou Institute of Geochemistry, Chinese Academy of Sciences, Guangzhou, Guangdong, China
[10]Centre for Star and Planet Formation, GLOBE Institute, University of Copenhagen, Copenhagen, Denmark
[11]Bayerisches Geoinstitut, Universität Bayreuth, Bayreuth, Germany
[12]Institut de Physique du Globe de Paris, CNRS, Université de Paris, Paris, France
[13]Department of Earth Science Education, Seoul National University, Seoul, Republic of Korea
[14]Department of the Geophysical Sciences and Enrico Fermi Institute, The University of Chicago, Chicago, Illinois, USA
[15]Faculty of Geosciences and Geography, University of Göttingen, Göttingen, Germany
[16]Faculty of Science, Ibaraki University, Mito, Japan
[17]ISAS/JSEC, JAXA, Sagamihara, Japan
[18]Department of Earth and Planetary Sciences, Tokyo Institute of Technology, Tokyo, Japan
[19]General Systems Studies, The University of Tokyo, Tokyo, Japan
[20]Earth and Planetary Sciences, Nagoya University, Nagoya, Japan
[21]Osaka Application Laboratory, SBUWDX, Rigaku Corporation, Osaka, Japan
[22]Max Planck Institute for Chemistry, Mainz, Germany
[23]Analytical Technology, Horiba Techno Service Co., Ltd., Kyoto, Japan
[24]Earth and Planetary Science, The University of Tokyo, Tokyo, Japan
[25]School of Earth and Environmental Sciences, The University of Queensland, St Lucia, Queensland, Australia
[26]Earth and Planetary Sciences, Kyoto University, Kyoto, Japan
[27]Geoscience, University of Wisconsin-Madison, Madison, Wisconsin, USA
[28]Max Planck Institute for Solar System Research, Göttingen, Germany
[29]Earth, Planetary, and Space Sciences, UCLA, Los Angeles, California, USA

[30]Lawrence Livermore National Laboratory, Livermore, California, USA
[31]Thermal Analysis, Rigaku Corporation, Tokyo, Japan
[32]Applied Chemistry, Tokyo University of Science, Tokyo, Japan
[33]Astromaterials Research and Exploration Science, NASA Johnson Space Center, Houston, Texas, USA
[34]Earth-System Sciences, Korea Polar Research Institute, Incheon, Korea
[35]Centre de Recherches Pétrographiques et Géochimiques, CNRS, Université de Lorraine, Nancy, France
[36]School of Earth and Space Sciences, University of Science and Technology of China, Anhui, China
[37]Department of Earth Sciences, Natural History Museum, London, UK
[38]Isotope Imaging Laboratory, Creative Research Institution, Hokkaido University, Sapporo, Japan
[39]Department of Earth Sciences, ETH Zurich, Institute for Geochemistry and Petrology, Zurich, Switzerland
[40]Earth and Space Science, Osaka University, Osaka, Japan
[41]Spectroscopy and Imaging, Japan Synchrotron Radiation Research Institute, Hyogo, Japan
[42]School of Earth and Space Exploration, Arizona State University, Tempe, Arizona, USA
[43]Geology, University of Maryland, College Park, Maryland, USA
[44]Graduate School of Natural Science and Technology, Okayama University, Okayama, Japan
[45]Earth and Planetary Sciences, University of California, Davis, California, USA
[46]Science and Engineering, National Museum of Nature and Science, Tsukuba, Japan
[47]Chemistry, Tokyo University of Science, Tokyo, Japan
[48]School of Earth Sciences and Engineering, Nanjing University, Nanjing, China
[49]Department of Earth Science, Tohoku University, Sendai, Japan
[50]Department of Earth and Planetary Sciences, Kyushu University, Fukuoka, Japan
[51]Earth and Planetary Systems Science Program, Hiroshima University, Higashi-Hiroshima, Japan
[52]Kanagawa Institute of Technology, Atsugi, Japan
[53]UTokyo Organization for Planetary and Space Science, University of Tokyo, Tokyo, Japan
Correspondence
J. Aléon, Institut de Minéralogie, de Physique des Matériaux et de Cosmochimie, Sorbonne Université, Museum National d'Histoire Naturelle, CNRS UMR 7590, IRD, Paris 75005, France.
Email: jerome.aleon@mnhn.fr

(Received 12 July 2023; revision accepted 15 January 2024)

Abstract–In order to gain insights on the conditions of aqueous alteration on asteroid Ryugu and the origin of water in the outer solar system, we developed the measurement of water content in magnetite at the micrometer scale by secondary ion mass spectrometry (NanoSIMS) and determined the H and Si content of coarse-grained euhedral magnetite grains (polyhedral magnetite) and coarse-grained fibrous (spherulitic) magnetite from the Ryugu polished section A0058-C1001. The hydrogen content in magnetite ranges between ~900 and ~3300 wt ppm equivalent water and is correlated with the Si content. Polyhedral magnetite has low and homogenous silicon and water content, whereas fibrous magnetite shows correlated Si and water excesses. These excesses can be explained by the presence of hydrous Si-rich amorphous nanoinclusions trapped during the precipitation of fibrous magnetite away from equilibrium and testify that fibrous magnetite formed from a hydrous gel with possibly more than 20 wt% water. An attempt to determine the water content in sub-μm framboids indicates that additional calibration and contamination issues must be addressed before a safe conclusion can be drawn, but hints at elevated water content as well. The high water content in fibrous magnetite, expected to be among the first minerals to crystallize at low water–rock ratio, points to the control of water content by local conditions of magnetite precipitation rather than large-scale alteration conditions. Systematic lithological variations associated with water-rich and water-poor magnetite suggest that the global context of alteration may be better understood if local water concentrations are compared with millimeter-scale distribution of the various morphologies of magnetite. Finally, the high water content in the magnetite precursor gel indicates that the initial O isotopic composition in alteration water must not have been very different from that of the earliest magnetite crystals.

INTRODUCTION

On December 6, 2020, the JAXA space mission Hayabusa2 returned 5.4 g from the type Cb carbonaceous asteroid 162173 Ryugu (Yada et al., 2022). This is the first successful sample return from a carbonaceous asteroid, an essential step in tying a link between carbonaceous meteorites and their parent asteroids, as well as understanding the origin of primitive volatile-rich materials in the solar system. The initial analysis campaign revealed that Ryugu is chemically, isotopically, and mineralogically related to Ivuna-type carbonaceous (CI) chondrites (Nakamura et al., 2023; Yokoyama et al., 2023). On one hand, the analyzed samples revealed extensive and pervasive aqueous alteration, but on the other hand they exhibit more primitive and reduced characteristics than CI chondrites, which seem to have suffered additional oxidation/modification on Earth. Isotopic analyses such as bulk Fe and Ni isotopes (Hopp et al., 2022; Spitzer et al., 2023) revealed unexpectedly unique properties indicating sampling from a previously unrecognized reservoir different from other carbonaceous chondrites. Evidence from CO_2-bearing fluid inclusions (Nakamura et al., 2023) and C isotopes in carbonates (Fujiya et al., 2023; McCain et al., 2023) suggest that this reservoir was located in the outer solar system, possibly beyond the CO_2 snow line. In situ oxygen isotopes in anhydrous minerals (Kawasaki et al., 2022; Liu et al., 2022) further suggest a link with cometary materials as sampled by the Stardust mission at comet Wild 2. Ryugu samples appear to be breccias containing clasts with varying degrees of alteration (Nakamura et al., 2023). Hence, Ryugu provides a unique sampling of outer solar system material possibly related to comets. Because minerals in the latter are dominantly anhydrous with volatiles present as ices, whereas Ryugu and CI chondrites consist of heavily hydrated lithologies, it is crucial to unravel the conditions of fluid circulation and water–rock interactions, which transformed a highly unequilibrated material into a rock dominated by minerals precipitated in the presence of an aqueous fluid such as phyllosilicates, iron oxides, sulfides, and carbonates.

Among these minerals, magnetite is a particularly sensitive tracer of fluid–rock interactions. Its properties can be used to shed light on water–rock ratios, redox conditions, and water origin. In Ryugu, magnetite appears to have the various morphologies commonly observed in CI chondrites, such as coarse-grained euhedral (hereafter polyhedral) grains, plaquette grains, radiating fibrous grains (also referred to as spherulites), and framboids (Dobrică et al., 2023; Kita et al., 2022; McCain et al., 2023; Nakamura et al., 2022, 2023; Yokoyama et al., 2023). Variable O isotopic compositions are observed in crystals large enough to be analyzed with a 5 µm lateral resolution, with $\Delta^{17}O$ mostly near 0‰ in polyhedral magnetite and positive $\Delta^{17}O$ ~2–3‰ in fibrous magnetite (Kita et al., 2022; McCain et al., 2023; Nakamura et al., 2022; Yokoyama et al., 2023). The Fe redox state as determined by synchrotron Mössbauer spectroscopy shows that Ryugu magnetites are pure Fe_3O_4, whereas they are more oxidized in the Orgueil CI chondrite and contain excess Fe^{III} (Viennet et al., 2022). Ryugu magnetite was characterized at the nanometer scale by transmission electron microscopy (TEM), with an emphasis on radiating fibrous spherulites (Dobrică et al., 2023). The latter were shown to have formed by precipitation away from equilibrium. Although magnetite is a nominally anhydrous mineral, in which hydrogen is not favorably incorporated, trace to minor amount of hydrogen may yield essential clues on the amount and composition of the aqueous fluid during magnetite precipitation. In order to gain insight on the formation of magnetite, as well as the nature and amount of aqueous alteration, we therefore developed a protocol for measurement of hydrogen content in magnetite by NanoSIMS and measured magnetite crystals from Ryugu having different morphologies and oxygen isotopic composition.

MATERIALS AND METHODS

Samples

Fourteen magnetite crystals (Table 1, Figure S1) were located in the polished section A0058-C1001, which was collected from the first touchdown site, allocated for this study. The sample was embedded in epoxy, gold coated, and previously described in Yokoyama et al. (2023). Ten of these magnetite grains have polyhedral morphologies and range in size between 10 and 15 µm (Figure 1). All grains are approximately equant. The remaining four grains have fibrous morphologies and range in size between 9 and 13 µm apart from grain 12, which is only 5 µm wide (G12 in Figure 1). Grain 7 is elongated but the other three fibrous grains have spherulitic morphologies. Six grains (five polyhedral and one fibrous) were previously analyzed for O isotopes by secondary ion mass spectrometry (SIMS, Table 1) and characterized by secondary electron microscopy (SEM) at Hokkaido University (Yokoyama et al., 2023). An attempt to determine H content was conducted on an aggregate of micrometer-sized magnetite microspherules adjacent to the fibrous grain 6 and to a plaquette magnetite grain (Figure 1). Distinction between aggregates of microspherules of variable granulometry, often filling voids, and strictly speaking framboidal magnetite consisting aggregates of sub-µm crystals of similar granulometry, sometimes spherical, sometimes euhedral, cohesive upon extraction from the matrix, is often made, for both Ryugu

TABLE 1. Properties of magnetite grains from Ryugu section A0058-C1001.

Grain #	Analysis	Morphology	Size (μm)	O isotopes[a]	$\Delta^{17}O$ (‰)[a]	2σ[a]	H_2O (wt ppm)	2σ	Si (wt ppm)	2σ	CG-phyllo[b]
Grain 6	HB_A58_06	Fibrous	12.2	mgt#6	3.1	1	2873	538	1749	681	N
	HB_A58_06bis_1	Fibrous		mgt#6	3.1	1	3339	638	2205	835	
Grain 7	HB_A58_07	Fibrous	12.8 × 14.8				2367	440	1226	579	N
Grain 12	HB_A58_12	Fibrous	4.9				1301	240	530	226	N
Grain 13	HB_A58_13	Fibrous	9.3				1688	304	1223	501	N
Grain 1	HB_A58_01	Polyhedral	10.0				1237	225	147	74	Y
	HB_A58_01bis	Polyhedral					1152	199	187	88	
Grain 2	HB_A58_02	Polyhedral	14.6	mgt#3	−0.3	1.2	1436	280	92	54	Y
	HB_A58_02bis_1	Polyhedral		mgt#3	−0.3	1.2	1070	184	131	75	
Grain 3	HB_A58_03bis	Polyhedral	14.5	mgt#4	0.5	0.9	1109	190	99	59	?
Grain 4	HB_A58_04	Polyhedral	14.9	mgt#8	−0.4	1.1	939	167	88	52	Y
	HB_A58_04bis	Polyhedral		mgt#8	−0.4	1.1	1017	189	102	58	
Grain 5	HB_A58_05	Polyhedral	14.5	mgt#1	−0.5	1.1	928	160	117	63	Y
	HB_A58_05bis	Polyhedral		mgt#1	−0.5	1.1	940	166	90	53	
Grain 8	HB_A58_08_1	Polyhedral	10.4	mgt#2	0.1	1.1	865	146	189	44	Y
Grain 9	HB_A58_09	Polyhedral	10.5 × 9.0				853	150	166	91	Y
Grain 10	HB_A58_10	Polyhedral	14.6				1033	183	208	99	Y
Grain 11	HB_A58_11	Polyhedral	12.2				949	168	153	77	Y
Grain 14	HB_A58_14	Polyhedral	12.7				978	170	93	54	Y

[a] Analysis number and O isotopic composition from Yokoyama et al. (2023).

[b] Coarse-grained phyllosilicate adhering to magnetite.

samples (Dobrică et al., 2023) and CI chondrites (Jedwab, 1971). As they are often found together (e.g., Figure 1, Hua & Buseck, 1998; Nakamura et al., 2022) and in the absence of a detailed characterization, they are hereafter referred to as microspherules/framboids (although variations in granulometry are noted within the imaged area, Figure 1).

NanoSIMS Standards

Several terrestrial magnetite crystals from the Sorbonne University mineral collection and of diverse provenance and geological context were polished by hand, embedded in indium, coated with 20-nm carbon, and analyzed in situ for H content, before and after NanoSIMS analysis, by Elastic Recoil Detection Analysis (ERDA) at the nuclear microprobe in Laboratoire d'Etude des Elements Légers - Nanosciences et Innovation pour les Matériaux, la Biomédecine et l'Energie (LEEL-NIMBE), using a $^{4}He^{+}$ microbeam of 3 × 12 μm at 2.7 MeV Energy, following established procedures (Bureau et al., 2009; Vangu et al., 2023) in order to produce suitable standards for determination of H concentrations. Three magnetite samples from Madagascar (#3664), Italy (Traversella, #3650), and Canada (Sudbury, #3649) (Table 2) were found (1) to yield areas with H content homogeneous enough to be used as standards for NanoSIMS analyses and (2) to be linearly correlated with the NanoSIMS secondary ion intensity ratios (Figure 2a). The elemental composition of the standards was determined by electron microprobe analysis (EMPA) using the SX5 electron microprobe from the CAMPARIS electron microprobe facility in Paris with a 15 keV and 40 nA electron current. Only the Sudbury magnetite was found to have Si content above the detection limits (~300 ppm, Figure 2b). Sudbury magnetite is composed of two different phases with differing H, Si, Mn, and Cl content. Repeated ERDA analyses show that H-poor areas have homogeneous H content (from 172 ± 17 to 234 ± 22 wt ppm H) yielding an average at 202 ± 31 wt ppm H. For normalization of Ryugu measurements, measurements of H contents were restricted to the H-poor area, considered here as an independent standard. Areas of the Madagascar magnetite free from inclusions and grain boundaries have been used both for ERDA and NanoSIMS. Although not completely homogeneous in ERDA within error, its range of H content is restricted enough (from 23 ± 3 wt ppm H to 43 ± 6 wt ppm H) and can be used for normalization with an average H content of 30 ± 11 wt ppm. Traversella magnetite exhibits a homogeneous H content of 50 ± 5 wt ppm H and contains only few inclusions that were carefully avoided in ERDA and NanoSIMS. Both Madagascar and Traversella magnetites, as well as H-poor sectors in Sudbury magnetite, are chemically homogeneous as determined by EMPA.

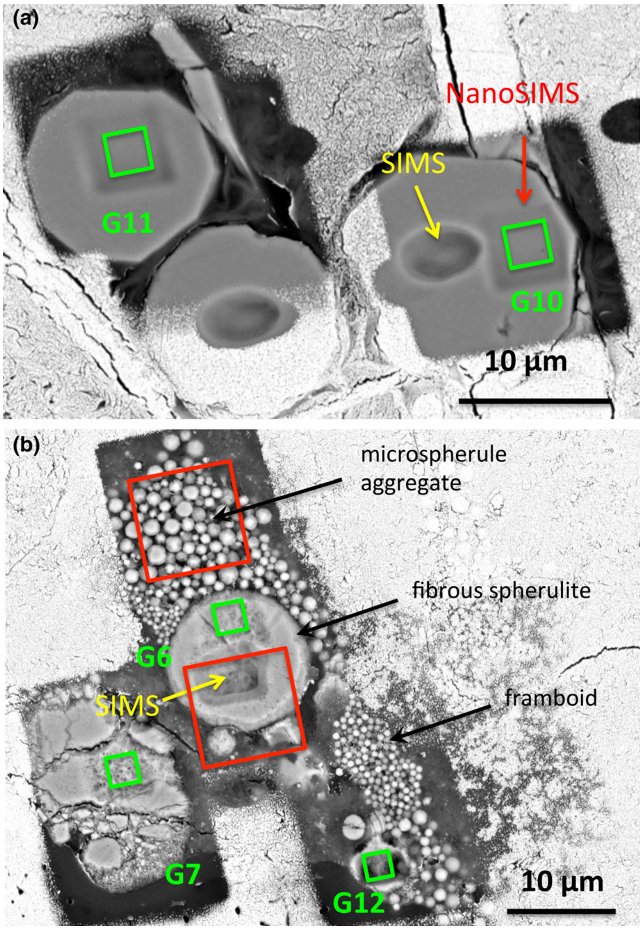

FIGURE 1. Petrographical context of NanoSIMS analyses. Backscattered electron images taken after SIMS and NanoSIMS analyses. (a) Coarse-grained euhedral magnetite. (b) Coarse-grained fibrous magnetite and microspherules/framboids. White coating around the sputtered area is Au coating. SIMS sputter pits are shown in yellow. Green squares: 2 × 2 µm central areas of NanoSIMS craters used for data analysis with the 80 pA beam. Red squares: 8 × 8 µm areas imaged by NanoSIMS with the 12 pA beam. Numbers of grains discussed in text and shown in detail in Figure S1 are given in green.

TABLE 2. Magnetite standards and compositions used for NanoSIMS calibration.

Sample	H (wt ppm)	SD	H_2O (wt ppm)	SD	Si (wt ppm)	Error mean
Madagascar #3664	30	11	268	98	106	25
Traversella #3650	50	5	447	45	103	55
Sudbury #3649, H-poor	202	31	1805	277	698	36

NanoSIMS Analysis

Analyses were conducted using the NanoSIMS 50 installed at Institut de Minéralogie, de Physique des Matériaux et de Cosmochimie—Museum National d'Histoire Naturelle (IMPMC-MNHN). Negative secondary ions $^{12}C^-$ or $^{13}C^-$, $^{16}OH^-$, $^{18}O^-$, $^{28}Si^-$, and $^{56}Fe^-$ were detected simultaneously on five electron multipliers. ^{12}C was initially chosen on the standards but was replaced by ^{13}C during the imaging of Ryugu grains where matrix adhering to the grains was more C rich. Ryugu grains measured initially with ^{12}C were remeasured with ^{13}C to ensure proper comparison with other grains and standards. The latter analyses are considered duplicate for H content. H contents were measured using $^{16}OH^-/^{18}O^-$ ratio (hereafter OH/O) and the calibration established by ERDA on magnetite standards (Figure 2a). Si contents were estimated using the $^{28}Si^-/^{56}Fe^-$ ratio (hereafter Si/Fe) and the standards as determined by EMPA (Figure 2b). The vacuum in the NanoSIMS analysis chamber was 2×10^{-9} Torr.

For magnetite grains larger than 5 µm, a 80 pA Cs^+ beam was rastered over 4 µm. A 1 µm blanking was applied so that only the central 2 × 2 µm area was used for analysis. For grains previously measured for O isotopes in Hokkaido University, targeted areas were established by removing the Au coating over an area slightly larger than each grain and using $^{16}OH^-$, $^{18}O^-$, and $^{56}Fe^-$ images acquired before analysis to locate areas larger than 4 µm adjacent to the Hokkaido O isotopes pits (Figure 1). Measurements were done using ES3 and AS2 entrance and aperture slits, respectively and with a 10% energy filtering. The mass resolving power was set to 5500, sufficient to resolve all interferences and have a flat OH peak top. Sputtering equilibrium was achieved after a 10 × 10 µm presputtering during 5 min, which also ensures minimal contamination together with using an intense primary beam during the measurements. The 5 µm fibrous magnetite grain 12 was measured twice using a 3 × 3 µm raster. Only the first analysis is reported here because the primary beam got through the grain before the end of the second analysis (Figure 1b).

Residual contamination of the sample that could come from adsorbed H from the vacuum or diffusing from H-rich areas of the sample (e.g., epoxy) was further monitored by ensuring that the ratios were not affected by changing the raster size from 3 to 8 µm, hence the sputtering rate, on the standards. This type of contamination, which depends on the measurement conditions rather than on the sample properties, is referred to as dynamic contamination. Lévy et al. (2019) demonstrated that dynamic contamination becomes significant when the sputtering rate decreases as raster

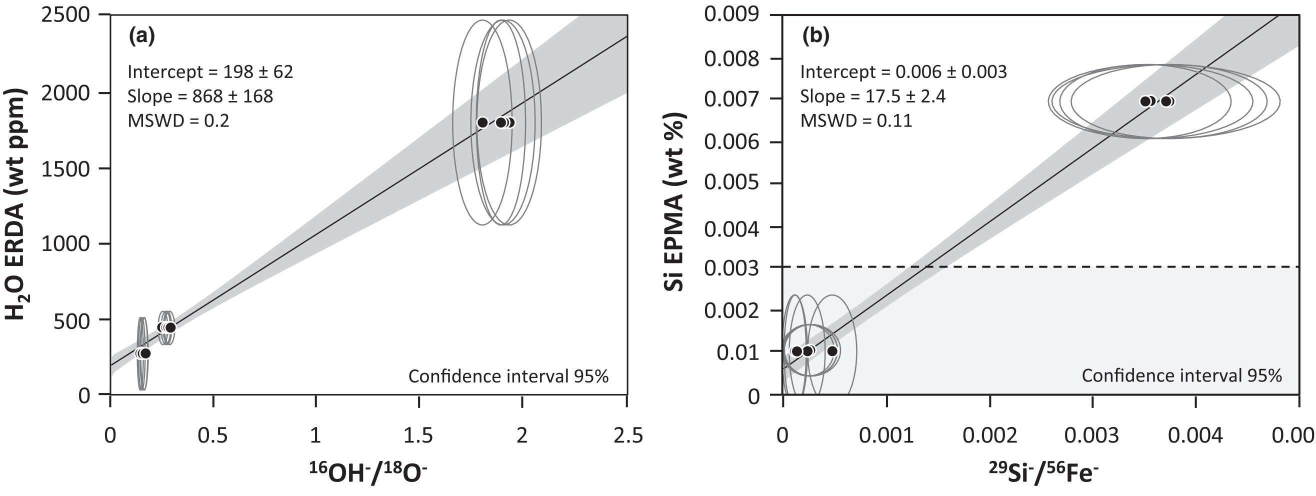

FIGURE 2. Calibrations used for the measurement of water content and Si content in magnetite with the 80 pA beam. (a) Calibration of water content using ERDA. (b) Calibration of Si content using EMPA. The gray area shows the detection limit for EMPA.

size increases. In amphiboles and with a 100 pA primary beam, it becomes significant above 10 μm. The $^{13}C^-/^{56}Fe^-$ ratio (hereafter C/Fe ratio) was used to monitor contamination from organics that could potentially be present in the analyzed areas, either due to the carbon coat on the standards or due to epoxy/indigenous organics on the A0058-C1001 section.

Error propagation includes internal error as well as uncertainties on the slope and intercept of the calibration line calculated with ERDA and NanoSIMS uncertainties using IsoplotR. All NanoSIMS uncertainties are standard deviations rather than standard error of the mean. The final relative uncertainty on the H content is between 17% and 20% (2 SD).

To determine H contents in μm-sized microspherules/framboids, the primary beam size was decreased to 12 pA (~170 nm) to allow scanning imaging of 8 × 8 μm areas with 256 × 256 pixels, while at the same time keeping the primary beam as intense as possible to minimize contamination. The Traversella standard and a Ryugu magnetite grain previously measured with the 80 pA beam (fibrous grain 6 adjacent to the microspherules, Figure 1b) were measured in the same conditions for normalization and comparison. To evaluate H contamination in these conditions, the dwell time was varied between 1 ms per pixel and 20 ms per pixel on the standard, again to vary the efficiency of sputtering (Lévy et al., 2019).

After NanoSIMS analysis, sputtered areas and craters were examined in backscattered and secondary electrons using the Tescan Clara field emission gun scanning electron microscope (FEG-SEM) from the MNHN electron microscopy facility to assess the validity of analyses (Figures 1 and 3 and Figure S1).

RESULTS

Contamination Monitoring and Small Beam Analysis

The lack of variations in measured OH/O ratios with raster size (Figure S2a) and the lack of correlation between OH/O ratios and C/Fe ratios (Figure S2b) ensured that contamination remained negligible during analyses with the 80 pA beam. Only the smallest fibrous grain (grain 12) had an elevated C signal but its H content remained the lowest among fibrous grains (see below). With the 12 pA beam, the secondary ion intensities are dominated by topography effects but large enough flat areas (620 nm to 1 μm wide) were found in the largest microspherules/framboids (Figure 4). With the 12 pA beam, OH/O ratios were on average higher by a factor 3.6–4.5 than those obtained with the 80 pA beam suggesting higher dynamic contamination with lower intensity (Stephant et al., 2014). However, the ratios varied little with dwell time and broadly consistent results were obtained in coarse-grained magnetite from the standards and Ryugu (Figure S3). This may indicate that the higher OH/O ratios are due to a variation in the secondary ion yields with the measurement conditions rather than contamination. More investigations are required for a robust evaluation of H content in microspherules or framboidal magnetite.

Coarse-Grained Magnetite

Two groups of H contents were found in Ryugu magnetite, correlated with morphology, Si content, and O isotopes (Table 1, Figure 5a). Polyhedral magnetite grains, five of which having $\Delta^{17}O$ ~0‰ (Yokoyama

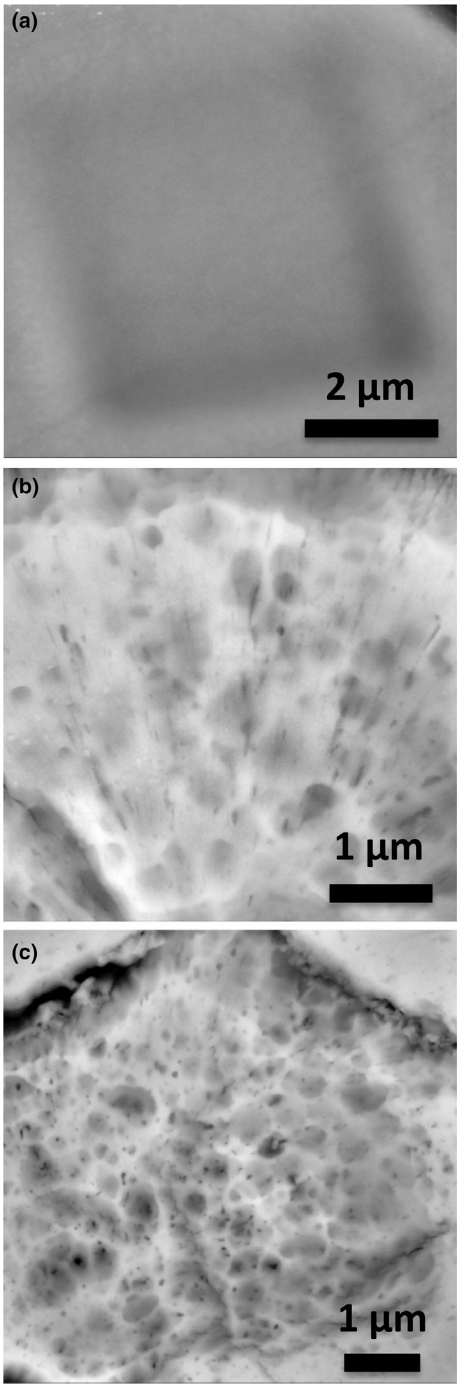

FIGURE 3. Backscattered electron micrographs of NanoSIMS analysis craters. (a) Whole crater from polyhedral magnetite grain 11. (b) Interior of crater from fibrous magnetite grain 6. (c) Interior of crater from fibrous magnetite grain 7.

et al., 2023), were found to be the most Si-poor and the most H-poor, with tightly grouped H contents between 853 ± 150 and 1436 ± 280 ppm equivalent H_2O by weight (2 SD). Si content in polyhedral magnetite ranges from 88 ± 52 to 208 ± 99 wt ppm (2 SD). Given the much higher sensitivity of the NanoSIMS at low content, these values remain below the detection limit of the electron microprobe analyses used for normalization (~300 wt ppm).

By contrast, four fibrous magnetite grains, one of which (grain 6) having $\Delta^{17}O = 3.1 \pm 1.0‰$ (2σ, Yokoyama et al., 2023), have higher Si content ranging from 530 to 2210 wt ppm and have H content ranging from 1301 ± 240 up to 3339 ± 638 wt ppm H_2O. Note that grain 12 with the highest C signal has both the lowest H and Si contents (1301 ± 240 ppm and 530 ± 226 ppm, respectively).

Duplicate measurements of four polyhedral magnetite and one fibrous magnetite yielded consistent results (Table 1) from 928 ± 160 and 940 ± 166 wt ppm H_2O at one end (grain 5) to 2873 ± 538 and 3339 ± 638 wt ppm H_2O at the other end (grain 6).

Morphologies of NanoSIMS Craters

Examination of NanoSIMS craters by FEG-SEM shows that polyhedral magnetite remained unchanged during sputtering (Figures 1 and 3). Crater edges are easily distinguished on SEM images and bottoms have a flat smooth morphology (Figure 3a). By contrast, fibrous magnetite became highly porous with significant topography upon sputtering, revealing nanoscale heterogeneities (Figure 3b,c) consistent with the occurrence of porosity and nanoinclusions, as described by TEM (Dobrică et al., 2023).

Aside from grain 3 where Au coating prevented observation of the phases adjacent to the magnetite crystals, a correlation is observed between magnetite morphology/H content and the morphology of phyllosilicates associated with and surrounding the grains. Polyhedral magnetite is systematically associated with coarse-grained phyllosilicates (Nakamura et al., 2023), which in some cases are adhering to the outer surface of the grain (Figures 1 and 6, grains G1, G5 and G9 in Figure S1). Larger scale SEM images acquired at Hokkaido University show that dolomite and coarse-grained platy pyrrhotite grains are also associated with this assemblage (Yokoyama et al., 2023), which appears to form veins and pockets in section A0058-C1001 (Figure 6). By contrast, the fibrous magnetite grains analyzed here are associated with the fine-grained matrix but never with coarse-grained phyllosilicates, which is also observed by TEM in other fragments from Ryugu (Dobrică et al., 2023).

DISCUSSION

Nature of H in Magnetite from Ryugu

The smooth craters lacking inclusions/fractures or grain boundaries in polyhedral magnetite suggest that H

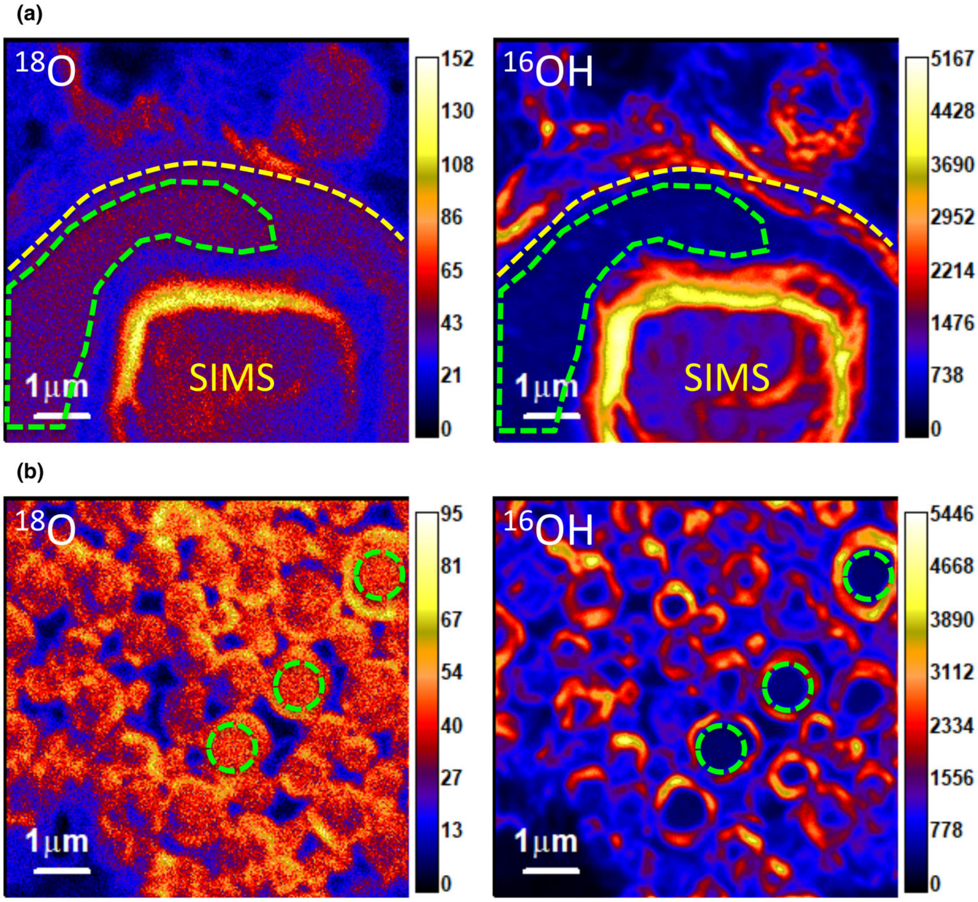

FIGURE 4. Ion images of fibrous magnetite and magnetite microspherules/framboids. (a) Fibrous magnetite 6. The dashed yellow line shows the edge of the grain. (b) Microspherule area in the vicinity (see Figure 1). Green dashed lines: regions of interest selected for data analysis. Ion intensities per pixel correspond to total counts.

in the latter is indigenous to the magnetite crystalline network. The measurements of magnetite standards indicate a detection limit ≤250 ppm equivalent H_2O for magnetite mounted in indium (Madagascar), much lower than the average 1000 ppm equivalent H_2O measured in polyhedral magnetite, which is therefore significant. Note nevertheless that the polished section A0058-C1001 was mounted in epoxy contrary to the standards. Epoxy has long been proposed to be a source of enhanced dynamic H contamination during SIMS and NanoSIMS analyses (Koga et al., 2003). Such a possible source of contamination is negligible for sample mounts extensively degassed, more than 3 weeks in high vacuum before analysis (Levy et al., 2019). However, due to allocation procedures during the initial analysis campaign, the A0058-C1001 section has been repeatedly analyzed in various SIMS and NanoSIMS laboratories and has only been degassed for the present work during 1 week in the storage chamber of the NanoSIMS prior to H analysis. Repeated SIMS analyses should in principle have resulted in extensive degassing of the section, but the efficiency of ingassing and surface contamination by adsorbed atmospheric water vapor during transport between the various SIMS sessions is unknown. Surface contamination due to degassing epoxy therefore remains a possible source of background H absent from the standards mounted in indium, which has to be investigated in detail. Still, such a possible residual contamination does not account for the correlation between H and Si content in fibrous magnetite showing the association between excess Si and excess H in fibrous magnetite relative to polyhedral magnetite.

This observed correlation can be interpreted as either (i) correlated incorporation of H and Si impurities within the magnetite crystalline network or (ii) a mixing between a Si-poor/Si-free component similar to that observed in polyhedral magnetite and a Si-rich, H-bearing component. The observation of higher Si content in the most H-rich standard magnetite Sudbury suggests that correlated impurities are a possibility. Indeed the Sudbury magnetite plots on the Ryugu fibrous magnetite correlation (Figure 5a). However, we note that Sudbury

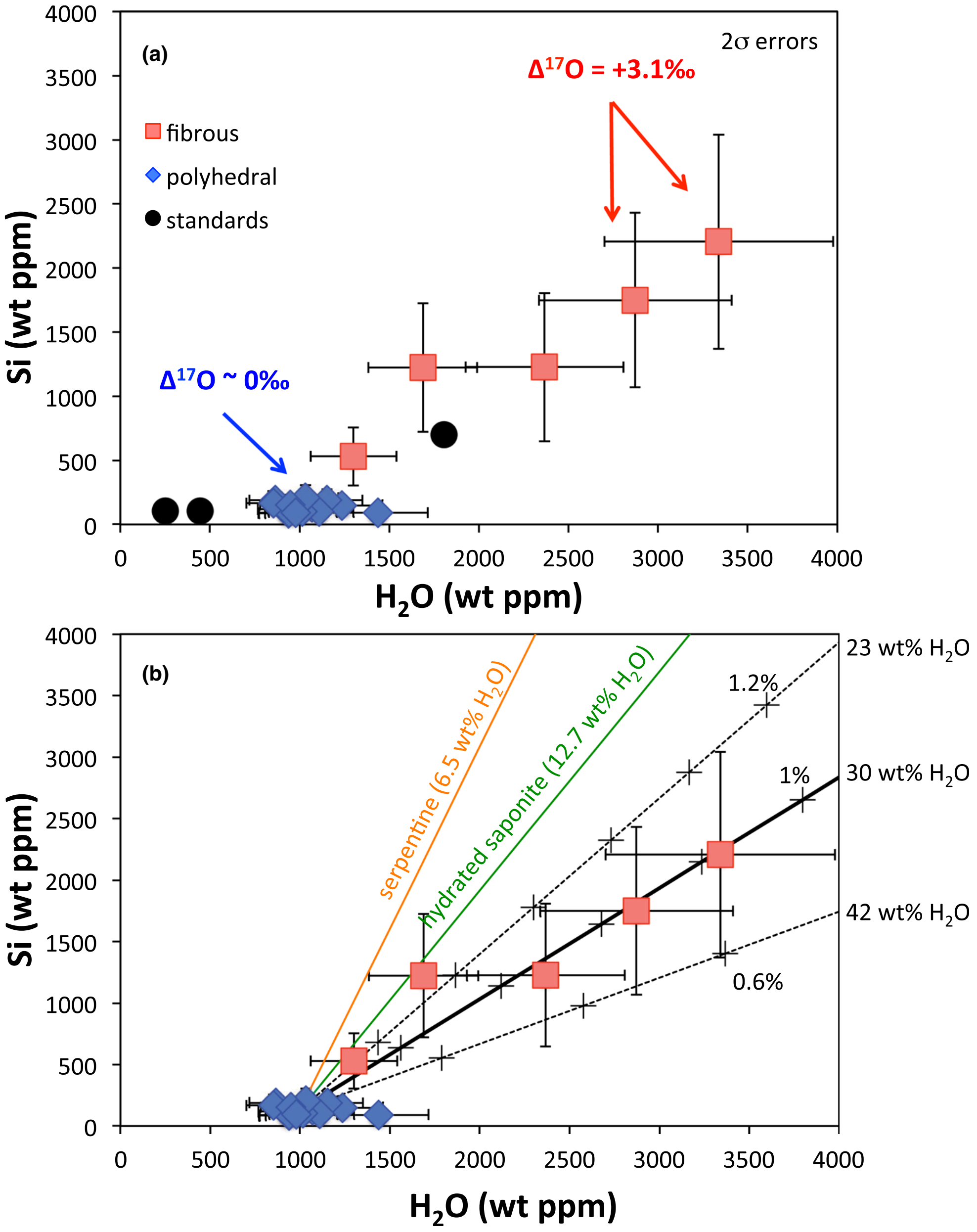

FIGURE 5. (a) Water content as a function of Si content in coarse-grained magnetite from Ryugu. Oxygen isotopic compositions are indicated. The two most water-rich analyses are repeat analyses of mgt grain 6. (b) Graphical representation of mixing calculations to evaluate the H_2O content of Si-rich nanoinclusions. Plain and dotted lines are mixing lines. Orange and green lines: mixing calculations using CI phyllosilicate compositions. Black lines: mixing calculations using the composition of the most Si-rich amorphous inclusions (type-b) in Dobrică et al. (2023). Numbers on the mixing lines indicate the mixing fraction of Si-rich inclusions. Uncertainties are 2 SDs.

magnetite is probably a shocked magnetite from the Sudbury impact crater and high amounts of Si and H in the crystalline network may possibly be a shock effect, not applicable to magnetite precipitated from aqueous fluids.

Alternatively, correlated H and Si contents associated with nanoscale heterogeneity revealed by ion sputtering in fibrous magnetite suggest that the higher H content could result from the presence of hydrated nano-silicates trapped during magnetite rapid growth rather than higher indigenous H content within the magnetite crystalline network. This hypothesis is supported by the TEM study of fibrous spherulitic magnetite from Ryugu, which revealed the systematic presence of nanoscale porosity within and between the elongated crystals that constitute radiating fibers in this type of magnetite (Dobrică

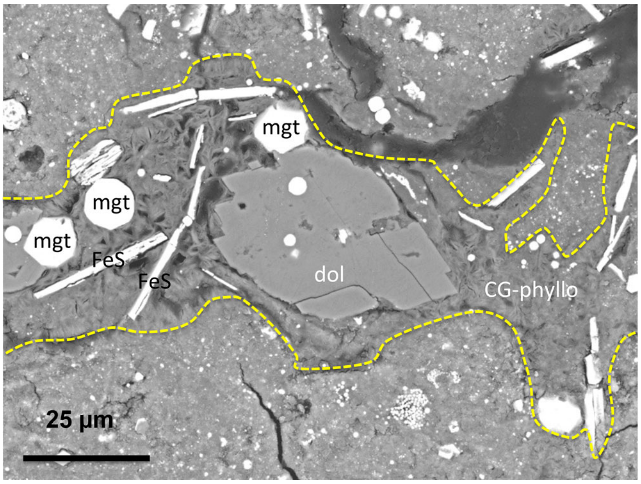

FIGURE 6. Backscattered electron image showing the mineralogical association of polyhedral magnetite with dolomite, coarse-grained phyllosilicates, and platy sulfides. The dashed yellow line shows the limit between this mineralogical association and regular matrix. mgt—magnetite, dol—dolomite, CG-phyllo—coarse-grained phyllosilicates, FeS—iron sulfides. Modified from Yokoyama et al. (2023).

et al., 2023). This porosity is often filled with amorphous Si-rich materials of variable composition. Three types of amorphous material composition have been recognized: Si-rich amorphous Fe oxide (type-a) within the fibers with 6.6 atom% Si (H_2O excluded), Fe-bearing amorphous silicate (type-b) within and between the fibers with 25.4 atom% of Si (H_2O excluded), and Mg-Fe-rich amorphous silicate (type-c) with 10.9 atom% Si (H_2O excluded) in inclusions elongated following the direction of the fibers and between the fibers (Dobrică et al., 2023). These Si-rich amorphous materials have been attributed to the trapping of gel-like material during the rapid growth of spherulitic magnetite away from equilibrium (Dobrică et al., 2023). Their systematic presence in fibrous magnetite and the strong textural similarity between TEM observations and SEM observations of NanoSIMS crater bottoms indicate that the observed correlation between Si and water content in fibrous magnetite is most likely due to the presence of these nanoinclusions in variable amount in the grains analyzed here. Minor discrepancies in pore textures and size distribution can be attributed to the preferential erosion of pore edges upon NanoSIMS sputtering. The possible elevated water content in microspherules/framboids suggested by imaging is also consistent with the TEM observations of nanopores in this morphology of magnetite (Dobrică et al., 2023).

Amount of Water in the Si-Rich Nanoinclusions

Our measurements therefore provide evidence that the amorphous Si-rich materials trapped in fibrous magnetite are hydrated, consistently with the gel-like materials expected from out-of-equilibrium magnetite growth (Dobrică et al., 2023; Kerridge et al., 1979). As a consequence, the correlation between Si and water content in Ryugu magnetite can be modeled as a mixing line resulting from the mixing of magnetite sensu stricto with little Si and H within the crystalline network and hydrated Si-rich nanoinclusions. In order to investigate whether the correlation could be explained by the contribution of minor amount of surrounding matrix material in the analyses rather than amorphous silicate nanoinclusions, we first calculated the mixing between a magnetite chemically identical to polyhedral magnetite and regular matrix phyllosilicates. Two phyllosilicate compositions were used: (1) a phyllosilicate with Si content identical to that of typical Orgueil serpentine (Tomeoka & Buseck, 1988) and water content consistent with Ryugu serpentine, that is, with water content corresponding to the bulk structural water (hydroxyls) in Ryugu phyllosilicates (6.5 wt%, Yokoyama et al., 2023) and (2) a phyllosilicate with Si content identical to that of typical Orgueil saponite (Tomeoka & Buseck, 1988) and water content consistent with hydrated saponite containing both structural and interlayer water as found in the bulk Ivuna CI chondrite (12.7 wt%, Yokoyama et al., 2023). Given that saponite in Ryugu is devoid of interlayer water contrary to CI chondrites (Nakamura et al., 2023; Viennet et al., 2023; Yokoyama et al., 2023), sampling hydrated saponite during analysis constitute an extreme water-rich unrealistic scenario. Figure 5b shows that none of these scenarios fit the observed correlation, thus ruling out the contribution of matrix material in our analyses. For such Si-rich materials, water content much higher than 12.7 wt% is required.

Using the Si content of the three types of amorphous materials reported in Dobrică et al. (2023) (see above), the correlation can be explained by the presence of 0.5%–5% amorphous material containing 5–40 wt% H_2O, the amount of water depending on the amount of Si. For the composition of type-a inclusions, this is 2.5%–5% material having 5–11 wt% H_2O, for the composition of type-b inclusions, this is 0.5%–1% material having 23–42 wt% H_2O, and for the composition of type-c inclusions, this is 1.2%–2.3% material having 10–21 wt% H_2O. The amount of inclusions needed is broadly consistent with the distribution of pores in fibrous magnetite, which account for about or less than 10% surface area in the TEM images in Dobrică et al. (2023). Note that both the amount of material and water content depend on the relative sensitivity factors (RSFs) used for the standardization of NanoSIMS data. We used the RSFs determined from the magnetite standards, but if H is indeed hosted mainly by amorphous silicate, the exact

RSF may be different. Due to an intricate mixture at a scale much smaller than that of the 80 pA primary beam (typically ~800 nm compared to ~100 nm inclusion size), a fully accurate determination of the RSF is extremely difficult given that in the OH/O ratio, most OH comes from the inclusions, whereas a large fraction of O comes from the surrounding magnetite. Similarly, for the Si/Fe ratio, Si comes mainly from the inclusions, whereas Fe comes mainly from magnetite. This uncertainty on the RSFs is, however, probably not larger than the uncertainty on our calculated concentrations arising from the variations in Si content and the analytical error. We therefore consider that the most Si-rich nanoinclusions contain probably between 10 wt% H_2O and possibly more than 20 wt%.

Insights on Fluid Circulations

Magnetite is the most abundant minor mineral in CI chondrites and Ryugu followed by pyrrhotite and carbonates (Alfing et al., 2019; Nakamura et al., 2023). The oxygen and carbon isotopic compositions of magnetite and carbonates have been extensively studied in order to shed light on their conditions of formation and on the origin and initial composition of the aqueous alteration fluids (Fujiya et al., 2023; Kita et al., 2022, 2023; McCain et al., 2023; Nakamura et al., 2022; Yokoyama et al., 2023). Both carbonates and magnetite have been found to have variable $\Delta^{17}O$ values varying between ~0‰ and ~ + 2‰, and between ~0‰ and +4‰, respectively. In a scenario, where the most primordial water of the solar system is enriched in ^{17}O and ^{18}O relative to ^{16}O and silicate dust (e.g., Sakamoto et al., 2007), the first mineral to crystallize from aqueous solutions would have ^{16}O deficits and thus elevated $\Delta^{17}O$ values relative to those crystallized after protracted equilibration with ^{16}O-enriched anhydrous silicates. Ca-carbonates (calcite) tend to have higher $\Delta^{17}O$ and $\delta^{18}O$ values, whereas dolomite has variable $\Delta^{17}O$ and $\delta^{18}O$ values and breunnerite grains have both the lowest $\Delta^{17}O$ and $\delta^{18}O$ values (Fujiya et al., 2023; Kita et al., 2023; McCain et al., 2023; Nakamura et al., 2022; Yokoyama et al., 2023), suggesting a crystallization sequence in the order calcite, dolomite, and finally breunnerite (Kita et al., 2023). A somewhat similar trend is found for magnetite with fibrous magnetite having systematically elevated $\Delta^{17}O$ and $\delta^{18}O$ values, whereas coarse-grained (>5 μm) euhedral magnetite has predominantly low $\Delta^{17}O$ values below +1‰ and systematically low $\delta^{18}O$ values (Kita et al., 2022; Yokoyama et al., 2023). A few exceptions have been found, where euhedral magnetite has $\Delta^{17}O$ values ≥ +1‰ but still has low $\delta^{18}O$ values (Kita et al., 2022). These distributions suggest that fibrous magnetite and calcite are among the first mineral to crystallize during aqueous alteration, whereas coarse-grained euhedral magnetite, most dolomite, and breunnerite formed later, after substantial isotopic equilibration of aqueous fluid with anhydrous silicates (Kita et al., 2022, 2023; McCain et al., 2023).

Textural relationships show that clasts enriched in anhydrous material found in Ryugu, corresponding to the least altered lithologies, contain magnetite spherules and calcite (Fujiya et al., 2023; Nakamura et al., 2023) that has not been observed to enclose magnetite. By contrast, dolomite not only occurs in the hydrated fine-grained matrix (Fujiya et al., 2023; Kita et al., 2023; McCain et al., 2023; Nakamura et al., 2022, 2023) but is also associated with coarse-grained phyllosilicates, platy sulfides, and coarse-grained euhedral magnetite (Kita et al., 2022, 2023; Yokoyama et al., 2023), defining structures resembling veins or isolated pockets (Figure 6). Dolomite commonly encloses magnetite, including magnetite plaquettes and framboids (McCain et al., 2023; Nakamura et al., 2022, 2023; Yokoyama et al., 2023). Among the various morphologies of magnetite, fibrous/spherulitic magnetite is commonly associated with microspherules aggregates, framboidal magnetite, and plaquettes (Figure 1, Dobrică et al., 2023; Nakamura et al., 2022, 2023), which is also observed in CI chondrites (e.g., Hua & Buseck, 1998). Although O-isotope analyses of magnetite microspherule aggregates and framboids are not available for Ryugu, microspherule/framboidal magnetite from a CI interplanetary dust particle (IDP) has $\Delta^{17}O$ ~ +3‰ (Aléon et al., 2009). This suggests that microspherule/framboidal magnetite, which was commonly found associated with fibrous spherulitic magnetite in Ryugu and CI chondrites (Figure 1 and Dobrică et al., 2023; Jedwab, 1971; Kerridge et al., 1979), shares geochemical properties with the latter, and formed in broadly similar conditions. Rare polyhedral magnetite with high $\Delta^{17}O$ values is also associated with fibrous magnetite (Kita et al., 2022).

Altogether, isotopic compositions, textures, and morphologies point to a multistage alteration with an early stage, where calcite and magnetite formed with the highest $\Delta^{17}O$ values, and a late stage with formation of most dolomite and most coarse-grained euhedral magnetite with $\Delta^{17}O$ ~0‰ (Fujiya et al., 2023; Kita et al., 2022, 2023; McCain et al., 2023). Note here that the bulk O isotopic composition of CI magnetite separate ($\Delta^{17}O$ of +1.6 to +1.8‰, Rowe et al., 1994) is close to the composition of fibrous magnetite in Ryugu and Ivuna (Kita et al., 2022; Yokoyama et al., 2023), indicating the minor contribution and occurrence of polyhedral magnetite at the rock scale and the early formation of most magnetite. Whether these stages correspond to a continuous evolution during alteration or to discrete events remains unclear. Based on the old ^{53}Mn-^{53}Cr age of late dolomite, McCain et al. (2023) concluded that ^{26}Al was still abundant during alteration. Carbon and O isotopes in carbonates further suggest that the first stage occurred during prograde alteration with increasing temperature, whereas the final stage took place during retrograde cooling (Fujiya et al., 2023; McCain et al., 2023). Finally, geochemical modeling indicates that water/rock mass ratios increasing from $\leq$0.1 up to 0.9 reproduce the observed mineralogical assemblages (Nakamura et al., 2023). These water/rock ratios correspond to equilibrium calculations and can be interpreted as an evolution of the bulk proportions of water and rock, in which case the correspondence of the predictions with lithological variations reflects a sequential evolution with increasing availability of water in bulk scale, for instance due to increasing ice melting. Alternatively, the equilibrium water/rock ratio can be interpreted in terms of local amount of rock having reacted with water, that is, the degree of alteration (Zolotov, 2012).

The evidence for trapping of hydrous gel nanoinclusions during the formation of fibrous magnetite raises questions on the former interpretation. Indeed, fibrous magnetite, the first magnetite to have formed, seems to have formed in the presence of abundant water. By contrast, the lower water content in coarse-grained euhedral magnetite may indicate a lower water/rock ratio in a later stage. At first glance, this suggests a decrease in the water/rock ratio during the progress of alteration, which could be expected from consumption of water during silicate hydration and progressive O isotopic equilibration of water with the anhydrous silicate matrix. However, as H content in magnetite appears to be principally related to the presence or absence of hydrous inclusions trapped during magnetite formation, it is probably a better indicator of equilibrium conditions during precipitation rather than water/rock ratio. Polyhedral magnetite may thus also have precipitated in the presence of a high amount of water, albeit in different conditions, much closer to equilibrium, in local veins or pocket of limited amplitude. The increasing water/rock ratios deduced from equilibrium calculations therefore probably reflects the increasing amount of water having locally reacted with the Ryugu protolith, rather than the temporal evolution of the bulk water abundance. In this case, excess water must have been removed rapidly or frozen to prevent the achievement of equilibrium in the little altered lithologies of Ryugu. Still, the limited abundance of the veins or pockets containing polyhedral magnetite may indicate a decreasing water/rock ratio at the bulk rock scale. Being less abundant at the bulk scale, water circulating in such veins or pockets would have experienced a larger degree of isotopic equilibration with silicates. In such a scenario, the bulk water/rock ratio would have been initially high due to ice melting and subsequently decreasing due to water consumption during hydration. Another possibility for the formation of these veins could be impact fracturation of the protolith and recirculation of expelled water having equilibrated O isotopes, associated with or after compaction and reduction of porosity and permeability. Indeed, early impact disruption to avoid overheating by ^{26}Al decay is a possible explanation for the old ^{53}Mn-^{53}Cr ages of dolomite (McCain et al., 2023). By contrast, the evidence for rapid precipitation out of equilibrium of fibrous magnetite may indicate an initially "open" and dynamic environment with fluid flow through connected porosity and limited isotopic equilibration between anhydrous silicates and water.

Implications for Early Solar System Water

The O isotopic composition of calcite at the onset of aqueous alteration and of fibrous magnetite formed (1) rapidly with limited interaction between water and anhydrous silicates in the early stages of aqueous alteration and (2) in the presence of a large amount of water suggesting that the initial alteration water had a Δ^{17}O value not much higher than the highest Δ^{17}O value measured in magnetite and calcite ($\sim +3‰$). As the Δ^{17}O value represents the excess or deficit of ^{16}O relative to the terrestrial mass fractionation of oxygen isotopes, it is independent from the magnetite–water mass fractionation and from the conditions of magnetite precipitation (e.g. temperature) and can be used a tracer of source. Being representative of the gel from which fibrous magnetite formed, the hydrous gel inclusions can be assumed to have a bulk Δ^{17}O value similar to their host magnetite. Mass balance considerations in a worst-case scenario, where this hydrous gel is assumed to consist of amorphous silicate having the stoichiometry of enstatite (as an approximation of an amorphous Mg-rich silicate precursor of CI chondrites) mixed with 10 wt% water, indicate that the atomic mixing proportions for O isotopes are 82% oxygen from silicate and 17% from water. In this case, the initial Δ^{17}O value of water was +18‰ if the Δ^{17}O value of the anhydrous silicate was initially 0‰. If instead the initial Δ^{17}O value of the silicate was similar to that of Ca-Al-rich inclusions (CAIs), the first solar system solids, at −25‰, the Δ^{17}O value of water must have been +139‰. If the hydrous gel was enriched in water with 25 wt% water (or if it was more silicate-poor, e.g., consisting of iron hydroxide gel with all O atoms derived from water), the initial Δ^{17}O value of water would have been +8‰ (or +48‰ in the case of CAI-like silicates). This shows that the Δ^{17}O value of water is consistent with that predicted from the extreme values found in cosmic symplectite in Acfer 094

(~ +90‰, Sakamoto et al., 2007) only if (i) the bulk silicate component was ^{16}O-enriched to the level of CAIs and (ii) water was not very abundant relative to silicate in the hydrous gel from which fibrous magnetite precipitated, which is an unlikely scenario. Indeed, the bulk initial anhydrous silicate probably has Δ^{17}O value barely negative, as suggested by the limited variations of O isotopic composition in anhydrous silicates of CI chondrites (Piralla et al., 2020) and by the composition of chondritic porous IDPs (Aléon et al., 2009; Nakashima et al., 2012; Starkey et al., 2014; Starkey & Franchi, 2013), which cluster near planetary O isotopic values (at 0‰) rather than solar (Δ^{17}O values ≤ −25‰ as found in CAIs). Additionally, we show here that water was indeed abundant in the gel inclusions relative to the silicate component. Therefore, the initial Δ^{17}O value of alteration water was probably not higher than about +10‰ (possibly up to +20‰). As the alteration fluids in Ryugu were CO_2-rich suggesting accretion in the outer solar system beyond the CO_2 snow line (Nakamura et al., 2023), this was probably the composition of water in this outer region of the protoplanetary disk. This implies that either the extremely anomalous composition of Acfer 094 cosmic symplectite (COS) is that of an exotic component not representative of the composition of the bulk water that circulated on planetary materials or an early pre-accretionary stage of O isotopic exchange and equilibration is required to lower the Δ^{17}O of nebular water to that of water in carbonaceous asteroids from the outer solar system. Limited ^{17}O and ^{18}O enrichments in the outermost Fe-oxide layer in COS (Matsumoto et al., 2022) suggest that the initial O isotopic composition of COS was modified in the Acfer 094 parent body by alteration fluids much closer in composition to typical planetary isotopic composition than COS, as found here for Ryugu. In line with the observation of $NaSO_4$ salts associated with COS (Matsumoto et al., 2022), Hashimoto and Nakano (2023) recently suggested that the formation of the cosmic symplectite may result from the peculiar chemistry of H_2SO_4. Low temperature gas-grain chemical reactions in the parent molecular cloud or the outer protoplanetary disk may have produced water reservoirs with heterogeneous O isotopic composition sampled differently by primitive bodies depending on the region of their parent body accretion.

CONCLUSION

The development of NanoSIMS analysis of water content in magnetite revealed different amounts of water in magnetite from asteroid Ryugu correlated with silicon content and associated with morphological and O isotopic differences. Fibrous spherulitic magnetites have elevated water content attributable to the trapping of amorphous nanoinclusions of hydrous silicon-rich gel from which magnetite precipitated far from equilibrium. By contrast, coarse-grained euhedral magnetite crystals exhibit lower water and silicon contents. These results show that early-formed magnetite crystallized in the presence of large amounts of water in spite of the low water–rock ratio expected at the bulk scale. This demonstrates that the geochemical and mineralogical properties of magnetite are better controlled by the local environment and the conditions of its precipitation rather than by the global conditions of alteration of Ryugu. The study of the distribution of the morphological types of magnetite at the millimeter scale in combination with this local information provides an alternative approach to understand the aqueous fluid circulations in Ryugu and other carbonaceous asteroids. The large amount of water required for magnetite formation at the onset of Ryugu alteration implies that the O isotopic composition of water during alteration evolved from a composition that was not too different from that of the earliest magnetite. Given the differences in magnetite morphologies and mineral associations, variations in the conditions of magnetite formation are expected during the progress of aqueous alteration. More work is clearly required for a better understanding of magnetite formation in CI chondrites and asteroid Ryugu and its implication for aqueous circulations.

Acknowledgments—This work was carried out under the Hayabusa2 Initial Analysis Team and the Chemistry subteam led by H. Yurimoto. We thank Sylvain Pont for assistance with the Clara TESCAN FEG-SEM at MNHN and Nicolas Rividi for help with the SX5 electron microprobe at the CAMPARIS facility. We also thank Yvan-Pierre Kilisky and Jim Hoarau for accelerator operation at the nuclear microprobe. Terrestrial magnetite samples were obtained from the mineral collection at UPMC; Jean-Claude Boulliard and Paola Giura are warmly thanked for their help with selection of the samples. We finally thank the reviewer Romain Tartèse, and Timothy Jull for editorial handling. The NanoSIMS at IMPMC was funded and is supported by MNHN, CNRS, and Région Ile-de-France. This work was supported by the French CNRS-INSU National Program of Planetology.

Conflict of Interest Statement—The authors declare no conflicts of interest.

Data Availability Statement—All data referred to in this article are given in the tables. Raw NanoSIMS, SEM EPMA, and ERDA data files are publicly available in the

Zenodo repository at https://doi.org/10.5281/zenodo.10419182.

Editorial Handling—Dr. A. J. Timothy Jull

REFERENCES

Aléon, J., Engrand, C., Leshin, L., and McKeegan, K. D. 2009. Oxygen Isotopic Composition of Chondritic Interplanetary Dust Particles: A Genetic Link between Carbonaceous Chondrites and Comets. *Geochimica et Cosmochimica Acta* 73: 4558–75.

Alfing, J., Patzek, M., and Bischoff, A. 2019. Modal Abundances of Coarse-Grained (>5 μm) Components within CI-Chondrites and their Individual Clasts—Mixing of Various Lithologies on the CI Parent Body(ies). *Geochemistry* 79: 125532.

Bureau, H., Raepsaet, C., Khodja, H., Carraro, A., and Aubaud, C. 2009. Determination of Hydrogen Content in Geological Samples Using Elastic Recoil Detection Analysis (ERDA). *Geochimica et Cosmochimica Acta* 73: 3311–22.

Dobrică, E., Ishii, H. A., Bradley, J. P., Ohtaki, K., Brearley, A. J., Noguchi, T., Matsumoto, T., et al. 2023. Nonequilibrium Spherulitic Magnetite in the Ryugu Samples. *Geochimica et Cosmochimica Acta* 346: 65–75.

Fujiya, W., Kawasaki, N., Nagashima, K., Sakamoto, N., Alexander, C. M. O'D., Kita, N. T., Kitajima, K., et al. 2023. Carbonate Record of the Change in Oxygen Fugacity and Gaseous Species in Asteroid Ryugu. *Nature Geoscience* 16: 675–682. https://doi.org/10.1038/s41561-023-01226-y.

Hashimoto, A., and Nakano, Y. 2023. Sulfuric Acid as a Corrosive Cryofluid and Oxygen Isotope Reservoir in Planetesimals. *Icarus* 398: 115535.

Hopp, T., Dauphas, N., Abe, Y., Aléon, J., Alexander, C. M. O'D., Amari, S., Amelin, Y., et al. 2022. Ryugu's Nucleosynthetic Heritage from the Outskirts of the Solar System. *Science Advances* 8: eadd8141.

Hua, X., and Buseck, P. R. 1998. Unusual Forms of Magnetite in the Orgueil Carbonaceous Chondrite. *Meteoritics & Planetary Science* 33: A215–A220.

Jedwab, J. 1971. La magnétite de la météorite d'Orgueil vue au microscope électronique à balayage. *Icarus* 15: 319–340.

Kawasaki, N., Nagashima, K., Sakamoto, N., Matsumoto, T., Bajo, K., Wada, S., Igami, Y., et al. 2022. Oxygen Isotopes of Anhydrous Primary Minerals Show Kinship between Asteroid Ryugu and Comet 81P/Wild2. *Science Advances* 8: eade2067.

Kerridge, J. F., Mackay, A. L., and Boynton, W. V. 1979. Magnetite in CI Carbonaceous Meteorites: Origin by Aqueous Activity on a Planetesimal Surface. *Science* 205: 395–97.

Kita, N. T., Kitajima, K., Kawasaki, N., Nagashima, K., Sakamoto, N., Yurimoto, H., and the Hayabusa2 Initial Analysis Chemistry Team, and the Hayabusa 2 Initial Analysis Core. 2023. High Precision SIMS Oxygen Isotope Analyses of Carbonates in Ryugu *54th Lunar and Planetary Science Conference*, abstract #1669.

Kita, N. T., Kitajima, K., Nagashima, K., Kawasaki, N., Sakamoto, N., Yurimoto, H., the Hayabusa2-Initial-Analysis Chemistry Team, and the Hayabusa2-Initial-Analysis Core. 2022. Oxygen Isotope Analyses of Magnetite in Ryugu *Hayabusa Symposium*, November 14–16, Sagamihara, Japan.

Koga, K., Hauri, E., Hirschmann, M., and Bell, D. 2003. Hydrogen Concentration Analyses Using SIMS and FTIR: Comparison and Calibration for Nominally Anhydrous Minerals. *Geochemistry Geophysics Geosystems* 4: 1019. https://doi.org/10.1029/2002GC000378.

Lévy, D., Aléon, J., Aléon-Toppani, A., Troadec, D., Duhamel, R., Gonzalez-Cano, A., Bureau, H., and Khodja, H. 2019. NanoSIMS Imaging of D/H Ratios on FIB Sections. *Analytical Chemistry* 91: 13763–71.

Liu, M.-C., McCain, K. A., Matsuda, N., Yamaguchi, A., Kimura, M., Tomioka, N., Ito, M., et al. 2022. Incorporation of ^{16}O-Rich Anhydrous Silicates in the Protolith of Highly Hydrated Asteroid Ryugu. *Nature Astronomy* 6: 1172–77.

Matsumoto, M., Tsuchiyama, A., Miyake, A., Ito, M., Matsuno, J., Uesugi, K., Takeuchi, A., Kodama, Y., Yasutake, M., and Vaccaro, E. 2022. Three-Dimensional Microstructure and Mineralogy of a Cosmic Symplectite in the Acfer 094 Carbonaceous Chondrite: Implication for its Origin. *Geochimica et Cosmochimica Acta* 323: 220–241.

McCain, K. A., Matsuda, N., Liu, M.-C., McKeegan, K. D., Yamaguchi, A., Kimura, M., Tomioka, N., et al. 2023. Early Fluid Activity on Ryugu Inferred by Isotopic Analyses of Carbonates and Magnetite. *Nature Astronomy* 7: 309–317.

Nakamura, E., Kobayashi, K., Tanaka, R., Kunihiro, T., Kitagawa, H., Potiszil, C., Ota, T., et al. 2022. On the Origin and Evolution of the Asteroid Ryugu: A Comprehensive Geochemical Perspective. *Proceedings of the Japanese Academy Series B* 98: 227–282.

Nakamura, T., Matsumoto, M., Amano, K., Enokido, Y., Zolensky, M. E., Mikouchi, T., Genda, H., et al. 2023. Formation and Evolution of Carbonaceous Asteroid Ryugu: Direct Evidence from Returned Samples. *Science* 379: eabn8671.

Nakashima, D., Ushikubo, T., Zolensky, M. E., and Kita, N. T. 2012. High Precision Oxygen Three-Isotope Analyses of Anhydrous Chondritic Interplanetary Dust Particles. *Meteoritics & Planetary Science* 47: 197–208.

Piralla, M., Marrocchi, Y., Verdier-Paoletti, M. J., Vacher, L. G., Villeneuve, J., Piani, L., Bekaert, D. V., and Gounelle, M. 2020. Primordial Water and Dust of the Solar System: Insights from In Situ Oxygen Measurements of CI Chondrites. *Geochimica et Cosmochimica Acta* 269: 451–464.

Rowe, M. W., Clayton, R. N., and Mayeda, T. K. 1994. Oxygen Isotopes in Separated Components of CI and CM Meteorites. *Geochimica et Cosmochimica Acta* 58: 5341–47.

Sakamoto, N., Seto, Y., Itoh, S., Kuramoto, K., Fujino, K., Nagashima, K., Krot, A. N., and Yurimoto, H. 2007. Remnants of the Early Solar System Water Enriched in Heavy Oxygen Isotopes. *Science* 317: 231–33.

Spitzer, F., Burkhardt, C., Kleine, T., and the Hayabusa2-Initial-Analysis Chemistry Team, and the Hayabusa2-Initial-Analysis Core. 2023. Nickel Isotopic Composition of Ryugu Samples Returned by the Hayabusa2 Mission. *54th Lunar and Planetary Science Conference*, abstract #2488.

Starkey, N. A., and Franchi, I. A. 2013. Insight into the Silicate and Organic Reservoirs of the Comet Forming Region. *Geochimica et Cosmochimica Acta* 105: 73–91.

Starkey, N. A., Franchi, I. A., and Lee, M. R. 2014. Isotopic Diversity in Interplanetary Dust Particles and Preservation of Extreme ^{16}O-Depletion. *Geochimica et Cosmochimica Acta* 142: 115–131.

Stephant, A., Remusat, L., Thomen, A., and Robert, F. 2014. Reduction of OH Contamination in Quantification of Water Contents Using NanoSIMS Imaging. *Chemical Geology* 380: 20–26.

Tomeoka, K., and Buseck, P. R. 1988. Matrix Mineralogy of the Orgueil CI Carbonaceous Chondrite. *Geochimica et Cosmochimica Acta* 52: 1627–40.

Vangu, D., Bureau, H., Khodja, H., Charrondière, M., Estève, I., Béneut, K., Remusat, L., Gaillou, E., Cartigny, P., and Boulliard, J. C. 2023. Combination of ERDA, FTIR Spectroscopy and NanoSIMS for the Characterization of Hydrogen Incorporation in Natural Diamonds. *Diamond and Related Materials* 136: 110007.

Viennet, J.-C., Roskosz, M., Beck, P., Alp, E. E., Lavina, B., Hu, M. Y., Zhao, J., et al. 2022. Iron Valence State and Mineralogy of Grains from Asteroid Ryugu. *53rd Lunar and Planetary Science Conference*, abstract #1834.

Viennet, J.-C., Roskosz, M., Nakamura, T., Beck, P., Baptiste, B., Lavina, B., Alp, E. E., et al. 2023. Interaction between Clay Minerals and Organics in Asteroid Ryugu. *Geochemical Perspective Letters* 25: 8–12.

Yada, T., Abe, M., Okada, T., Nakato, A., Yogata, K., Miyazaki, A., Hatakeda, K., et al. 2022. Preliminary Analysis of the Hayabusa2 Samples Returned from C-Type Asteroid Ryugu. *Nature Astronomy* 6: 214–220.

Yokoyama, T., Nagashima, K., Nakai, I., Young, E. D., Abe, Y., Aléon, J., Alexander, C. M. O'D., et al. 2023. Samples Returned from the Asteroid Ryugu are Similar to Ivuna-Type Carbonaceous Meteorites. *Science* 379: eabn7850.

Zolotov, M. Y. 2012. Aqueous Fluid Composition in CI Chondritic Materials: Chemical Equilibrium Assessments in Closed Systems. *Icarus* 220: 713–729.

SUPPORTING INFORMATION

Additional supporting information may be found in the online version of this article.

Figure S1. Secondary electron images of coarse-grained magnetite grains analyzed by NanoSIMS.

Figure S2. Sensitivity of OH/O ratios to contamination. (a) OH/O ratio as a function of raster size on Sudbury magnetite standard showing the lack of relationship with sputtering rate and thus with surface contamination.

Figure S3. Comparison of ion yields between intense beam spot analysis (80 pA) and small beam imaging (12 pA) using the OH/O ratios.

Figure S4. Graphical representation of mixing calculations to evaluate the H_2O content of Si-rich nanoinclusions using the composition of the Si-rich inclusions in Dobrică et al. (2023).